Robotica (2025), **43**, pp. 3959–3975
doi:10.1017/S026357472510266X

CAMBRIDGE UNIVERSITY PRESS

RESEARCH ARTICLE

Robust control based on Lyapunov stability theory for the joint modules in hip-assist exoskeleton robots

Xiaoli Liu[1,2], Youli Hu[1], Faliang Wang[3], Shengchao Zhen[2,3] and Ye-Hwa Chen[4]

[1]School of Artificial Intelligence, Anhui University, Hefei, Anhui, PR China
[2]Human-Computer Collaborative Robot Joint Laboratory of Anhui Province, Hefei, Anhui, PR China
[3]School of Mechanical Engineering, Hefei University of Technology, Hefei, Anhui, PR China
[4]The Geroge W.Woodruf School of Mechanical Engineering, Georgia Institute of Technology, Atlanta, Georgia, USA
Corresponding author: Faliang Wang; Email: faliang941118@163.com

Received: 13 December 2024; **Revised:** 30 April 2025; **Accepted:** 5 September 2025; **First published online:** 13 October 2025

Keywords: hip-assist exoskeleton robot; robust control; joint module; disc motor; Lyapunov method

Abstract

This paper presents a novel robust control method for a hip-assist exoskeleton robot's joint module, addressing dynamic performance under variable loads. The proposed approach integrates traditional PID control with robust, model-based strategies, utilizing the system's dynamic model and a Lyapunov-based robust controller to handle uncertainties. This method not only enhances traditional PID control but also offers practical advantages in implementation. Theoretical analysis confirms the system's uniform boundedness and ultimate boundedness. A Matlab prototype was developed for simulation, demonstrating the control scheme's feasibility and effectiveness. Numerical simulations show that the proposed fractional-order hybrid PD (FHPD) controller significantly reduces tracking error by 58.70% compared to the traditional PID controller, 55.41% compared to the MPD controller, and 32.32% compared to ADRC, highlighting its superior tracking performance and stability.

1. Introduction

As the population ages, there is a decline in the physical capabilities of the elderly, notably a decrease in their ability to walk, increasing the demand for mobility-assisting medical devices. Lower limb exoskeleton robots, as intelligent mechatronic systems, effectively assist elderly individuals with limited mobility through human-computer interaction technology, aiding them in performing daily activities such as climbing stairs and providing support on uneven terrain.

Beyond healthcare, exoskeleton robots also play a role in military and rescue operations, enhancing strength and endurance to allow soldiers to carry heavy equipment and adapt to complex environments. In labor-intensive industries, they reduce the physical strain on workers, improve efficiency, and lower the risk of work-related injuries [1]. Joint actuation control lies at the heart of precise movement in exoskeleton robots, and devising control strategies for diverse application scenarios presents a significant research challenge, as shown in Figure 1. The adaptive robust control algorithm proposed in this paper aims to enhance the dynamic performance and stability of hip-assist exoskeleton robots, catering to the walking needs of a variety of users.

The drive control of exoskeleton robots is fundamental to ensuring stability and precise positional control. Given the complexity of their structure, mere low-level control is insufficient for the coordinated actuation required in complex operational environments [2]. Therefore, it is essential to integrate advanced upper-level control strategies into the exoskeleton robot's control system. This integration will enhance the robot's motion accuracy, adaptability, and safety, thereby expanding its range of applications and increasing its value. Disc motors, noted for their torque richness, swift reactions, and space-saving form, optimally power the joints in these exoskeletons. Their design allows concentration of high power

© The Author(s), 2025. Published by Cambridge University Press.

https://doi.org/10.1017/S026357472510266X Published online by Cambridge University Press



Figure 1. *Wearing a hip-assist exoskeleton robot.*

in a small area, key to creating sturdy and compact mechanisms for hip-assist devices. Disc motors' efficiency and quiet operation both contribute to better device performance and a more pleasant user experience [3]. With ongoing technological progress, the integration of disc motors in such exoskeletons is likely to broaden, promising more sophisticated and effective support for elderly mobility. Such advancements may notably improve the elderly's daily living standards and overall well-being [4].

Development of these robots' joint mechanisms faces uncertainties due to variations in system parameters and external elements. Uncertainties in motor specifications, such as torque constants and inertia, along with the gear ratios of harmonic drive reducers, can lead to discrepancies from projected models [5]. Moreover, the joint dynamics can be affected by external variables, including shifting loads, unstable temperatures, and operational inconsistencies. As these factors can impact the dynamic performance of the joint units, ongoing research aims to refine control strategies to ensure reliable and consistent operation of hip-assist exoskeleton robots [6].

In classical control theory, PID control is widely recognized for its effectiveness in servo control systems, attributed to its straightforward structure and ease of parameter tuning [7]. Despite its long-standing success, PID control faces challenges when applied to modern servo systems that demand high

https://doi.org/10.1017/S026357472510266X Published online by Cambridge University Press

dynamic response speeds, precise steady-state accuracy, and superior disturbance rejection capabilities [8]. These systems often require control strategies that offer enhanced nonlinear compensation and improved parameter robustness.

Currently, several advanced control strategies have been explored for servo control systems. One such approach is Active Disturbance Rejection Control (ADRC). ADRC employs an extended state observer to estimate and compensate for disturbances in real-time [9]. A key advantage of ADRC is its reduced reliance on precise mathematical models [10]. However, its practical application can be influenced by the balance between observer bandwidth and noise sensitivity, and its multi-parameter coupling may require careful tuning [11].

Sliding mode control is known for its ability to ensure finite-time convergence of system states through predefined sliding surfaces [12]. This method offers strong robustness by effectively suppressing matched disturbances. Yet, the high-frequency oscillations associated with switching functions can lead to chattering, which may accelerate actuator wear and potentially excite unmodeled dynamics [13]. These characteristics present considerations for its use in high-precision servo systems.

Predictive control is another strategy that addresses multi-constrained problems by employing receding horizon optimization [14]. Its effectiveness is closely tied to the accuracy of the prediction model. In applications sensitive to time delays, such as hip-assist exoskeletons, there is a notable trade-off between the algorithm's real-time performance and dynamic response. Achieving precise acceleration tracking remains a challenge in these scenarios [15].

To ensure precise trajectory following and robust dynamic reactions in the unpredictable nonlinear dynamics of systems like hip-assist exoskeleton robots, we've crafted a resilient control strategy founded on a definitive model, termed fractional-order hybrid PD (FHPD) control. This approach, while maintaining a straightforward architecture, delivers reliable control outcomes despite the presence of system uncertainties [16, 17]. The deterministic robust control system we've introduced effectively tackles and regulates these uncertainties through the strategic use of the joint module's elements and design specifications.

Our framework initially categorizes system behavior into predictable and probabilistic segments, addressing joint module uncertainties within a bounded function. We integrate robust deterministic techniques with PID control, ensuring alignment with the system's kinetic properties and resilience against unmodeled dynamics and parameter variations. Utilizing Lyapunov methods [18, 19], we establish the controller's stability, offering a simpler and more resource-efficient design suitable for constrained engineering applications.

This paper is structured into sections that cover the joint module's nonlinear dynamics [20], the development and stability analysis of our robust control approach, comparative performance evaluations with PID and MPD controllers, and a conclusion summarizing key research outcomes.

2. Dynamic system modeling

In the domain of dynamic assessment [21], the hip-assist exoskeleton robot's joint module is conceptualized as a composite unit, featuring a harmonic drive reducer coupled with a disc motor. Equation (1) captures the mathematical essence of the disc motor's dynamics:

$$\begin{cases} \dot{i}_d = -\dfrac{R}{L_d} i_d + \dfrac{L_q}{L_d} n_p \dot{q} i_q + \dfrac{u_d}{L_d} \\ \dot{i}_q = -\dfrac{R}{L_q} i_q - \dfrac{L_d}{L_q} n_p \dot{q} i_d - n_p \dot{q} \dfrac{\Psi_f}{L_q} + \dfrac{u_q}{L_q} \\ \ddot{q} = \dfrac{T_e}{J} - \dot{q} \dfrac{B}{J} - \dfrac{T_p}{J} \end{cases} \tag{1}$$

Within the scope of this study, the variables i_d and i_q are indicative of the stator currents along the direct and quadrature axes, respectively. Correspondingly, u_d and u_q, denote the stator voltages in the d-axis and q-axis directions. The inductances of the stator along these axes are represented by L_d and

https://doi.org/10.1017/S026357472510266X Published online by Cambridge University Press

L_q. The term n_p signifies the count of pole pairs, ω symbolizes the angular velocity of the rotor, and Ψ_f refers to the flux linkage in the rotor. The stator resistance is denoted by R. Furthermore, parameters B, T_e, and T_p are associated with the mechanical dynamics of the disc motor, relating to rotational inertia, damping due to viscosity, the torque generated by electromagnetic force, and the torque applied by the load, respectively.

Upon examining Eq. (1), it becomes evident that there is a nonlinear relationship between the speed and armature current of the disc motor. By decoupling Eq. (1), the derivation of the electromagnetic torque T_e is presented as follows:

$$T_e = \frac{3}{2} n_p i_p \left[\psi_f + (L_d - L_q) i_d\right] \tag{2}$$

In the propulsion system of a disc motor, the Field-Oriented Control (FOC) technique is extensively applied. By aligning the vector sum of the three-phase stator currents along the q-axis, the d-axis current i_d is nullified, with the q-axis current i_q equating to the total current i_s. Controlling the q-axis current i_q in accordance with the principles of FOC allows for direct influence over the electromagnetic torque, which in turn optimizes dynamic responses due to the autonomous regulation of torque. The mathematical model for an embedded disc motor is delineated in Eqs. (3) and (4), serving as the theoretical foundation. For the surface-mounted disc motor used in experiments, it is assumed that the d-axis and q-axis inductances L_d and L_q are equal, collectively denoted as L. Thus, the mathematical model characterizing the surface-mounted disc motor is as follows:

$$\begin{cases} \dot{i}_d = 0 \\ \dot{i}_q = -\dfrac{R}{L_q} i_q - n_p \dot{q} \dfrac{\psi_f}{L_q} + \dfrac{u_d}{L_d} \\ \ddot{q} = \dfrac{\tau}{J} - \dot{q} \dfrac{B}{J} - \dfrac{T_q}{J} \end{cases} \tag{3}$$

The expression for the electromagnetic torque T_e is as follows:

$$T_e = \frac{3}{2} n_p \psi_f i_q = K_n i_q \tag{4}$$

Within this framework, K_n is designated as the constant of torque. By examining Eq. (3), the motion equation for the disc motor is articulated in the subsequent manner:

$$J\ddot{q} + B\dot{q} + T_p = T_e \tag{5}$$

The movement of the manipulator's joints is regulated by the motor's output shaft through a harmonic drive reducer. The focus is on examining the operational transmission efficiency and the gear ratio of the reducer. The dynamic equation for the harmonic drive reducer can be succinctly represented as follows:

$$T_N = \mu \eta T_p \tag{6}$$

The constants μ and η correspond to the gear ratio and the efficiency of the harmonic drive reducer, respectively. T_N signifies the torque that the load imparts on the joint assembly. After integrating Eqs. (5) and (6) and taking into account the friction forces present in the harmonic drive reducer, the dynamic equation for the joint assembly is derived as follows:

$$J\ddot{q} + B\dot{q} + \frac{T_N}{\mu \eta} + T_f = T_e \tag{7}$$

Within the harmonic drive reducer, the nonlinear frictional torque T_f has a decisive impact on the dynamic performance of the joint module. The academic community continues to work on developing mathematical models of friction forces, aiming to more accurately assess the specific impact of these forces on the overall performance of mechanical systems, and has proposed various models to mitigate their adverse effects. In this study, we focus on introducing two types of friction models [22]: first, the widely recognized standard Coulomb friction model, followed by an optimized Stribeck model that

https://doi.org/10.1017/S026357472510266X Published online by Cambridge University Press

incorporates factors such as initial friction, Coulomb friction, viscous resistance, and velocity transitions to more comprehensively reflect the friction characteristics within the joint module. Next, the key features of the standard Coulomb viscous friction model will be further elaborated [23]:

$$T_f = f_b\dot{q} + f_d sgn(\dot{q}) \tag{8}$$

The improved Stribeck friction model is articulated as follows [24]:

$$T_f = \left[f_d + (f_s - f_d)\theta^{-(\frac{\dot{q}}{\dot{q}s})^2}\right] sgn(\dot{q}) + f_b\dot{q} - f_g \tag{9}$$

In the formula, f_b represents the parameter for viscous friction, f_d denotes the parameter for Coulomb friction, and f_s is the parameter for static friction. The symbol $\dot{q}s$ is associated with the measure of lubrication. To counteract the irregular variations in frictional force that may occur during changes in the direction of motion, the element f_g is incorporated into the model, the detailed function of which will be further elaborated in subsequent discussions:

$$\begin{cases} f_g = s\theta^{-\frac{\dot{q}^2}{v}} \\ s = sgn(\dfrac{\dot{q}}{a})f_s + f_d l \\ v = a\dot{q}_s(d * sgn(a) + c * sgn(\dot{q})) \end{cases} \tag{10}$$

In this context, l, d and c represent the gain factors, while a corresponds to the acceleration $\ddot{q}$. The subsequent steps illustrate the transformation of Eq. (7) into its Lagrangian formulation:

$$E(q,t)\ddot{q} + I(q,\dot{q},t)\dot{q} + G(q,\dot{q}) + F(q,\dot{q},t) = \tau(t) \tag{11}$$

where

$$\begin{cases} E = \dfrac{J}{K_n} \\ I = \dfrac{B}{K_n} \\ G = 0 \\ F = \dfrac{T_n}{\mu\eta} + T_f \\ \tau = i_q \end{cases} \tag{12}$$

Given that the subject of our study is a solitary disc motor, functioning as a mechanical system with a single degree of freedom, the variable in question is unidimensional. As the disc motor is designed for rotational movement only, the function G(·) equates to zero.

3. The robustly designed control system

3.1. The development of a resilient control framework

Our aim is for the mechanical system to accurately follow the preset trajectory $q^d(t)$ with a desired swift velocity $\dot{q}^d(t)$, assuming $q^d(t)$ is defined on $[t_0, \infty]$ with continuous second-order differentiability, and both $q^d(t)$, its first derivative $\dot{q}^d(t)$, and second derivative $\ddot{q}^d(t)$ are uniformly bounded:

$$\begin{cases} \theta(t) = q(t) - q^d(t) \\ \dot{\theta}(t) = \dot{q}(t) - \dot{q}^d(t) \\ \ddot{\theta}(t) = \ddot{q}(t) - \ddot{q}^d(t) \end{cases} \tag{13}$$

Let:

$$\widetilde{\theta}(t) = \left[\theta(t)\dot{\theta}(t)\right]^T \tag{14}$$

https://doi.org/10.1017/S026357472510266X Published online by Cambridge University Press

Our objective is to ensure that the system's state variable $\widetilde{\theta}(t)$ remains uniformly bounded under the control of the developed controller and ultimately achieves uniform ultimate boundedness. The dynamics of the joint module, as defined by Eq. (11), can be reconceptualized as follows:

$$E(\ddot{q}^d(t) + \ddot{\theta}(t)) + I(\dot{q}^d(t) + \dot{\theta}(t)) + F = \tau(t) \tag{15}$$

In fact, due to the uncertainty and variability of parameters, as well as the dynamic characteristics not fully described by the model, the system inherently contains uncertainty. Therefore, the dynamic model can be decomposed into a standard part and an uncertain part. The division of the functions $E(\cdot)$, $I(\cdot)$ and $F(\cdot)$ can be understood in the following manner:

$$\begin{aligned} E(q,\sigma,t) &= \overline{E}(q,t) + \triangle E(q,\sigma,t) \\ I(q,\dot{q},\sigma,t) &= \overline{I}(q,\dot{q},t) + \triangle I(q,\dot{q},\sigma,t) \\ F(q,\dot{q},\sigma,t) &= \overline{F}(q,\dot{q},t) + \triangle F(q,\dot{q},\sigma,t) \end{aligned} \tag{16}$$

In this context, $\overline{E}(\cdot)$, $\overline{I}(\cdot)$ and $\overline{F}(\cdot)$ denote the baseline components, whereas the variations ΔE, ΔI and ΔF signify the oscillating elements correlated with σ.

Subsequently, the estimated range of uncertainty and external disturbances is denoted by the variable ρ. For a given positive value of S, the scalar function ρ is chosen in a manner that:

$$\left\| \phi(\theta,\dot{\theta},\sigma,t) \right\| \leqslant \rho(\theta,\dot{\theta},\sigma,t) \tag{17}$$

where:

$$\begin{aligned} \phi(\theta,\dot{\theta},\sigma,t) = &-\triangle E(q,\sigma,t)(\ddot{q}^d - S\dot{\theta}) - \triangle I(q,\dot{q},\sigma,t)(\dot{q}^d - S\theta) \\ &- \triangle F(\dot{q},\sigma,t) \end{aligned} \tag{18}$$

The subsequent goal is to devise an efficient control strategy $\tau(t)$ that ensures the tracking error is confined within predefined limits. We can utilize an algorithm to guarantee the desired performance constraints [25]. With a positive value of ϵ (typically small) and positive tuning coefficients k_p and k_v, the control law for the nonlinear system can be derived as follows:

$$\tau(t) = \overline{E}(\ddot{q}^d - S\dot{\theta}) + \overline{I}(\dot{q}^d - S\theta) + \overline{F} - K_p\theta - K_v\dot{\theta} + p(\theta,\dot{\theta},t) \tag{19}$$

where

$$p(\theta,\dot{\theta},t) = \begin{cases} -\dfrac{\varphi(\theta,\dot{\theta},t)}{\epsilon}\rho(\theta,\dot{\theta},t), & if\ \left\|\varphi(\theta,\dot{\theta},t)\right\| \leqslant \epsilon \\ -\dfrac{\varphi(\theta,\dot{\theta},t)}{\left\|\varphi(\theta,\dot{\theta},t)\right\|}\rho(\theta,\dot{\theta},t), & if\ \left\|\varphi(\theta,\dot{\theta},t)\right\| > \epsilon \end{cases} \tag{20}$$

$$\varphi(\theta,\dot{\theta},t) = (\dot{\theta} + S\theta)\rho(\theta,\dot{\theta},t) \tag{21}$$

$$K_p = diag\left[K_{pi}\right]_{n*n} \tag{22}$$

$$K_v = diag[K_{vi}]_{n*n} \tag{23}$$

Through in-depth analysis, our proposed model-based PD robust control framework demonstrates a design that relies on accurate system modeling and fully leverages the advantages of the PID control mechanism. The proportional adjustment component of the controller is designed to neutralize external disturbances and system uncertainties, with its piecewise design effectively preventing an excessive increase in robustness as the control signal decreases. This theoretical framework suggests that the FHPD controller surpasses standard PID and MPD controllers in terms of dynamic response. Figure 2 comprehensively displays the controller configuration, explaining how model-driven components and the

https://doi.org/10.1017/S026357472510266X Published online by Cambridge University Press

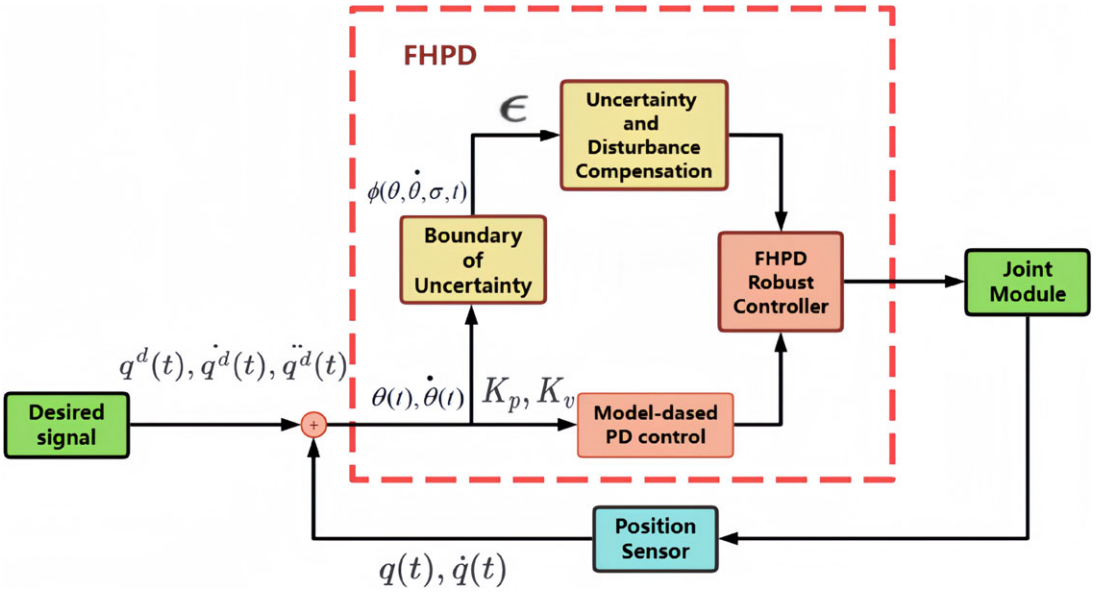


Figure 2. *Proposed FHPD robust control architecture diagram.*

PD feedback loop work together to reduce the discrepancy between the target and actual positions. In addition, the proportional component effectively alleviates uncertainties from the mechanical system and external disturbances, significantly enhancing the system's dynamic performance.

After structural analysis of the proposed controller, its advantages can be rephrased as follows:

1. Our algorithm, an extension of the traditional PD control, simplifies the complexity of parameter adjustment for engineering applications, enhancing its practicality.
2. The algorithm not only streamlines the parameter tuning process but also demonstrates robustness against uncertainties in parameters and external disturbances.
3. With a design that emphasizes simplicity and ease of implementation, the controller requires minimal hardware resources, making it suitable for a variety of mechanical systems with common embedded chips.

The design process of the PD robust controller for the joint module system can be re-articulated as:

Step one: Establish the dynamic equation of the joint module system using the Lagrangian approach.

Step two: Determine the upper bounds of external disturbances and uncertainties within the system, and calculate the scalar function q through Eq. (17).

Step three: Construct a piecewise function for q based on Eqs. (20) and (21).

Step four: Develop a model-based PD robust control method according to Eq. (19).

Considering the comprehensive analysis of the controller and its design process, it is notable that our proposed controller, with its low hardware requirements and ease of adjusting control parameters, is not only applicable to motor-driven systems but can also be rapidly adapted and integrated into various types of mechanical systems to achieve the desired motion control effects.

3.2. Stability analysis

Theorem. The controller (19) maintains the joint module's error term $\widetilde{\theta}\ (t)$ within a predefined boundary and ensures its convergence to a steady state within this boundary. The selection of an appropriate value for ϵ allows for the minimization of the error's steady-state boundary, aligning with the precision objectives.

https://doi.org/10.1017/S026357472510266X Published online by Cambridge University Press

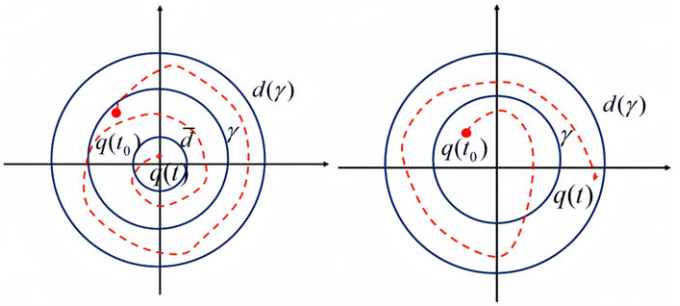


Figure 3. *System performance.*

1. Uniform boundedness: For any $\gamma > 0$,there exists a finite $d(\gamma)$ such that the norm of $q(t)$ does not exceed $d(\gamma)$ for all times t greater than or equal to t_0, provided that the initial condition $\|q(t_0)\|$ is less than or equal to γ, $\|q(t) \leqslant d(\gamma)\|$ for all $t \geqslant t_0$, as shown in the left part of Figure 3.
2. Uniform ultimate boundedness: Given $\gamma > 0$, if the initial condition $\|q(t_0)\|$ is within the bound γ, there exists a positive d such that the norm of $q(t)$ will be at least d for all future times t beyond $t_0 + T(\bar{d}, \gamma)$, where $T(\bar{d}, \gamma)$ is a finite time that depends on $\bar{d}$ and γ, $\|q(t)\| \geqslant d$ for all $t \geqslant t_0 + T(\bar{d}, \gamma)$ with $\bar{d} > d$ and $T(\bar{d}, \gamma) < \infty$, as shown in the right part of Figure 3.

Proof. By employing the Lyapunov minimax approach, the stability assessment of the proposed controller is executed. Functions $d(r)$ and $\bar{d}$ are established to ensure the system's uniform boundedness and ultimate boundedness, enabling the closed-loop system to achieve the target error threshold in a finite timeframe. In the process of substantiating the controller's stability, the subsequent discussion elaborates on the criteria for selecting an appropriate Lyapunov function candidate:

$$V(\widetilde{\theta}, t) = \frac{1}{2}(\dot{\theta} + S\theta)^T E(\dot{\theta} + S\theta) + \frac{1}{2}\theta^T(K_p + SK_v)\theta \tag{24}$$

The Hamiltonian function $E(q)$ of the mechanical system is confirmed to be uniformly positive definite, indicating the presence of a constant δ that satisfies this condition:

$$E(q) \geqslant \delta I \quad \forall q \in R^n \tag{25}$$

To verify that V is a Lyapunov function, it is necessary to demonstrate that V is both positive definite and monotonically decreasing [26]. Given that Eq. (25) ensures the boundedness of E, the analysis can proceed as follows:

$$\begin{aligned} V(\widetilde{\theta}, t) &\geqslant \frac{1}{2}\delta \left\|\dot{\theta} + S\theta\right\|^2 + \frac{1}{2}\theta^T(K_p + SK_v) \\ &= \frac{1}{2}\delta(\theta^2 + 2S\dot{\theta}\theta + S^2\theta^2) + \frac{1}{2}\delta(K_p + SK_v)\theta^2 \\ &= \frac{1}{2}[\theta\dot{\theta}]\psi[\theta\dot{\theta}] \end{aligned} \tag{26}$$

where

$$\psi = \begin{bmatrix} \delta + K_p + SK_v & \delta S \\ \delta S & \delta \end{bmatrix} \tag{27}$$

Demonstrating that ψ is positive is straightforward, which confirms that V is positive definite.

$$V \geqslant \frac{1}{2}\lambda_{min}(\psi)(\theta^2 + \dot{\theta}^2) \geqslant \frac{1}{2}\underline{\lambda}\|\theta\|^2 \tag{28}$$

where $\underline{\lambda} = min\ \lambda_{min}(\psi)$, $\underline{\lambda} \geqslant 0$. This indicates that V is positive definite.

https://doi.org/10.1017/S026357472510266X Published online by Cambridge University Press

The change rate of V along the trajectory can be outlined as follows:

$$\begin{aligned}\dot{V} &= (\dot{\theta} + S\theta)^T(\tau - E\ddot{q}^d - I(\dot{\theta} + \dot{q}^d) - F + ES\dot{\theta}) \\ &\quad + \frac{1}{2}(\dot{\theta} + S\theta)^T\dot{\theta}(\dot{\theta} + S\theta) + \theta^T(K_p + SK_v)\dot{\theta} \\ &= (\dot{\theta} + S\theta)^T(\tau - E(\ddot{q}^d - S\dot{\theta}) - I(\dot{q}^d - S\theta) - F) \\ &\quad - (\dot{\theta} + S\theta)^T I(\dot{\theta} + S\theta) + \frac{1}{2}(\dot{\theta} + S\theta)^T\dot{E}(\dot{\theta} + S\theta) \\ &\quad + \theta^T(K_p + SK_V)\dot{\theta} \end{aligned} \tag{29}$$

By Eq. (19) and using Eq. (29),

$$\begin{aligned}\dot{V} &= (\dot{\theta} + S\theta)^T[(\overline{E} - E)(\ddot{q}^d - S\dot{\theta}) + (\overline{I} - I)(\dot{q}^d - S\theta) \\ &\quad + \overline{F} - F + p] - (\dot{\theta} + S\theta)^T(K_p e + K_v\dot{\theta}) + \theta^T(K_p + SK_v)\dot{\theta} \\ &= (\dot{\theta} + S\theta)^T\phi + (\dot{\theta} + S\theta)^T p - \dot{\theta}^T K_v\dot{\theta} - \theta^T SK_p\theta \end{aligned} \tag{30}$$

if $\|\varphi\| > \epsilon$, then

$$(\dot{\theta} + S\theta)^T p = -\frac{(\dot{\theta} + S\theta)^T(\dot{\theta} + S\theta)\rho}{\|\varphi\|}\rho = -\|\varphi\| \tag{31}$$

if $\|\varphi\| \leqslant \epsilon$, then

$$(\dot{\theta} + S\theta)^T p = -\frac{(\dot{\theta} + S\theta)^T(\dot{\theta} + S\theta)\rho}{\|\epsilon\|}\rho = -\frac{\|\varphi\|^2}{\epsilon} \tag{32}$$

Therefore, by Eqs. (21), (31) and (32), we get,

$$(\dot{\theta} + S\theta)^T\phi + (\dot{\theta} + S\theta)^T p \leqslant (\dot{\theta} + S\theta)^T p + \|\varphi\| \tag{33}$$

If $\|\varphi\| > \epsilon$ (31), we are able to derive

$$(\dot{\theta} + S\theta)^T p + (\dot{\theta} + S\theta)^T\phi \leqslant 0 \tag{34}$$

If $\|\varphi\| \leqslant \epsilon$ (32), we are able to derive

$$\frac{\epsilon}{4} \geqslant \|\varphi\| - \frac{\|\varphi\|^2}{\epsilon} \geqslant (\dot{\theta} + S\theta)^T\phi + (\dot{\theta} + S\theta)^T p \tag{35}$$

Consequently, when $\epsilon > 0$, inequality (35) is valid for all ϵ. Substituting (35) into Eq. (30) yields the following result:

$$\frac{\epsilon}{4} - \underline{\lambda}_1\left\|\widetilde{\theta}\right\|^2 \geqslant \dot{V} \tag{36}$$

where

$$\underline{\lambda}_1 = min\left\{K_v, SK_p\right\} \tag{37}$$

Actually, for all norms $\left\|\widetilde{\theta}\right\|$ that meet the specified criteria, the value of V will be negative:

$$\frac{\epsilon}{4} - \underline{\lambda}_1\left\|\widetilde{\theta}\right\|^2 < 0 \tag{38}$$

The purpose of these properties is to ensure the consistency of the boundary. In other words, for any given $\gamma > 0$ and $\left\|\tilde{\theta}\left(t_0\right)\right\| \leqslant \gamma$ (where t_0 represents the initial time), the following inequality always

https://doi.org/10.1017/S026357472510266X Published online by Cambridge University Press

holds:

$$d(r)=\begin{cases} R\left[\dfrac{2(\overline{\lambda}_0+\overline{\lambda}_1 R+\overline{\lambda}_2 R^2)}{\underline{\lambda}}\right]^{\frac{1}{2}}, & if\ \ r\leqslant R \\ r\left[\dfrac{2(\overline{\lambda}_0+\overline{\lambda}_1 r+\overline{\lambda}_2 r^2)}{\underline{\lambda}}\right]^{\frac{1}{2}}, & if\ \ r>R \end{cases} \tag{39}$$

$$R=\left[\frac{\epsilon}{4\underline{\lambda}_1}\right]^{\frac{1}{2}} \tag{40}$$

Uniform ultimate boundedness can be guaranteed, meaning that $\left\|e\left(t\right)\right\|$ will not exceed $d\left(r\right)$ for all $t\geqslant t_0$. Essentially, this holds true for any given $\bar{d}$:

$$\overline{d}>R\left[\frac{2(\overline{\lambda}_0+\overline{\lambda}_1 R+\overline{\lambda}_2 R^2)}{\underline{\lambda}}\right]^{\frac{1}{2}} \tag{41}$$

By employing the following methods, the system's performance can be guaranteed [27]:

$$T(\overline{d},r)=\begin{cases} 0, & if\ \ r\leqslant\overline{R} \\ \dfrac{\overline{\lambda}_0 r^2+\overline{\lambda}_1 r^3+\overline{\lambda}_2 r^4-\frac{1}{2}\underline{\lambda}\overline{R}^2}{\underline{\lambda}\overline{R}^2-\frac{\epsilon}{4}}, & if\ \ r\geqslant\overline{R} \end{cases} \tag{42}$$

$$\overline{R}=r_2^{-1}\left(\frac{1}{2}\underline{\lambda}\overline{d}^2\right) \tag{43}$$

$$r_2(\zeta)=\overline{\lambda}_0\zeta^2+\overline{\lambda}_1\zeta^3+\overline{\lambda}_2\zeta^4 \tag{44}$$

By choosing a suitably, the size of the terminal bounded region [28] can be made arbitrarily small for all $t\geqslant t_0+T\left(\bar{d},r\right)$, provided that $\left\|\tilde{\theta}\left(t\right)\right\|\leqslant\bar{q}$.

3.3. Simulation

This paper employs numerical simulation to assess the efficacy of the robust elastic control strategy. Key parameters of the disc motor are detailed in Table I, which are then used to calculate Eq. (11), yielding the matrix in Eq. (15) that forms the basis for the simulation analysis.

In assessing the relative performance of PID, MPD, ADRC and FHPD in position tracking tasks, we utilized both step and sinusoidal inputs for our experiments, facilitating a comprehensive evaluation of the data obtained.

After thorough testing of the control parameters for three algorithms to ensure a fair comparison and to find a balance between system stability and response speed, we determined the optimal parameter settings as shown in Table II. In the simulation of the FHPD control strategy, the uncertainty introduced by the cosine function had a relatively minor impact on the disc motor.

However, when the motor was subjected to sinusoidal disturbances, the impact was significantly greater compared to square wave disturbances. Based on this finding, we decided to adopt the formula $\hat{F}=0.5+0.01*\sin\left(5t\right)$ to represent the uncertainty factor of the motor. The initial error $e\left(\circ\right)$ was set to zero at the start of the experiment, and a fixed sampling interval of 0.001 s was chosen.

1. Step Response Test: The amplitude of the step signal, denoted as q^d, is set to 51.0556°. The corresponding results are displayed in Figure 4. It was noted that the FHPD controller achieved

https://doi.org/10.1017/S026357472510266X Published online by Cambridge University Press

Table I. *Constituents and variables of the joint module mechanism.*

Emblem	Representation	Preset value
q (degree)	θ_{jm}	–
J (kg · m^2)	I_{jm}	1.65×10^{-3}
B (Nm/rad/s)	μ_{motor}	9×10^{-3}
λ	TR of HR	101
η	TE of HR	0.95
ψ_f (V/rad/s)	ψ_{rotor}	2.5×10^{-2}
n_p	p_{motor}	6

Table II. *Variables within control strategies.*

Control system	Control coefficient
PID	$K_p = 90$, $K_i = 5$, $K_d = 8$
MPD	$K_p = 70$, $K_d = 8$
ADRC	$\omega_0 = 16$, $\omega_c = 2$, $K_p = 100$, $K_i = 6$, $K_d = 8$
FHPD	$K_p = 90$, $K_v = 8$, $\epsilon = 0.001$

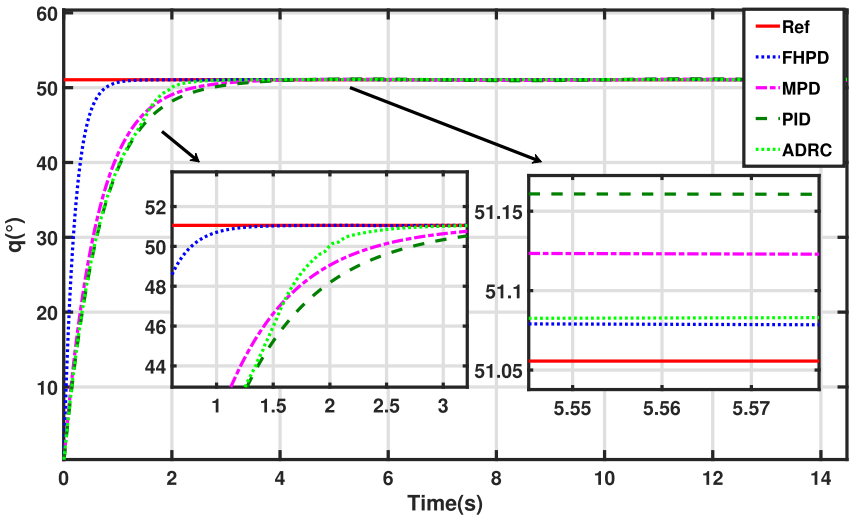


Figure 4. *Disc motor's sine wave tracking simulation results.*

the target trajectory more swiftly and without any overshoot, outperforming both the PID and MPD controllers.

2. Sinusoidal Signal Tracking: The sinusoidal signal is considered as the reference path for tracking with amplitude 80.6686°.

Figures 5 presents the simulation results for a sinusoidal signal tracking scenario using a Stribeck friction model. The system's initial response to the sinusoidal signal was similar to that of a step input scenario. Upon reaching a steady state, the FHPD controller demonstrated a reduction in steady-state error and a shorter time to recovery compared to the PID and MPD controllers, exhibiting a swifter return to stability. The findings from these simulations indicate that the discussed controller is effective in enhancing the system's dynamic response capabilities.

https://doi.org/10.1017/S026357472510266X Published online by Cambridge University Press

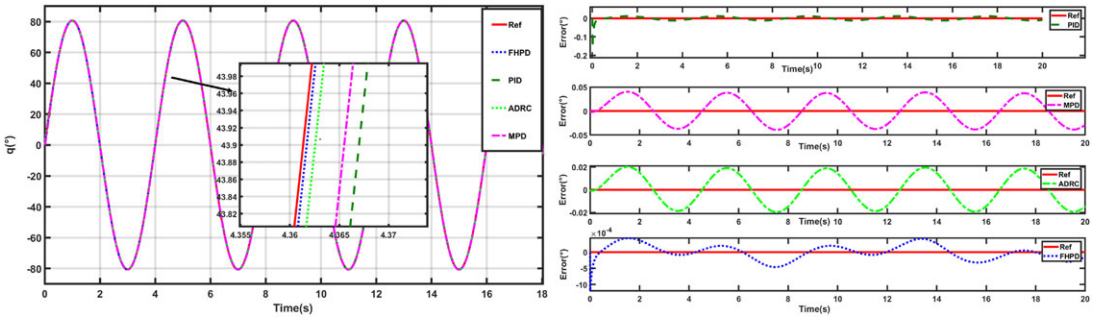


Figure 5. *Sinusoidal signal tracking.*

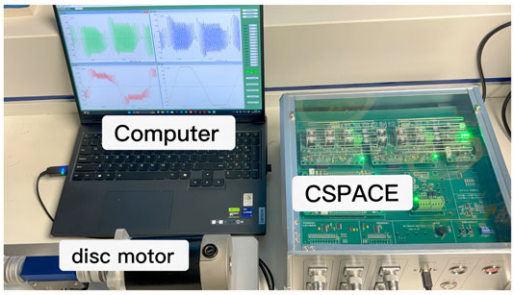


Figure 6. *The experimental platform known as CSPACE.*

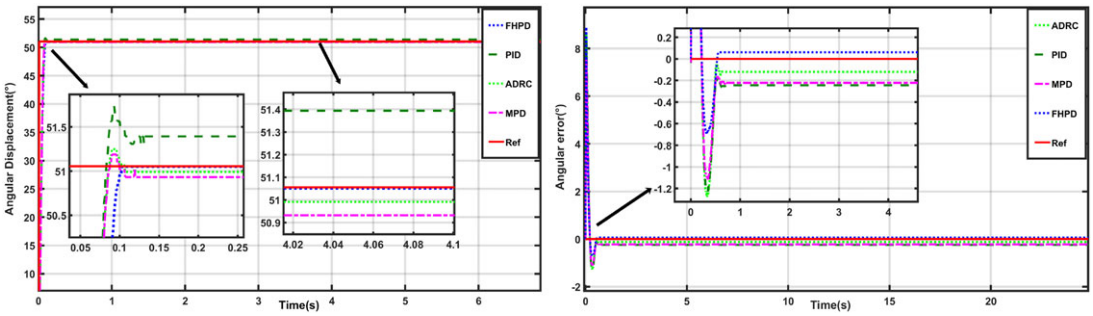
3.4. Experiment

A series of experiments focusing on the disc motor have been conducted to thoroughly verify the applicability of the control algorithm. As depicted in Figure 6, the experimental setup includes a computer, cSPACE supervisory software, a cSPACE control unit, and a disc motor embedded in a hip-assisting exoskeleton robot, among other equipment. An encoder with a 2500-line incremental count capability is utilized to collect positional data of the motor, with the simulation tests employing identical parameter settings.

The experimental procedure consists of three main stages: Firstly, the positional signals of the motor are acquired by the incremental encoder and fed back to the controller; Secondly, the digital signal processor within the cSPACE system, in accordance with our proposed control strategy, receives and processes the incoming data; Lastly, the motor is driven by augmenting the control signal, thereby achieving precise motion control of the disc motor.

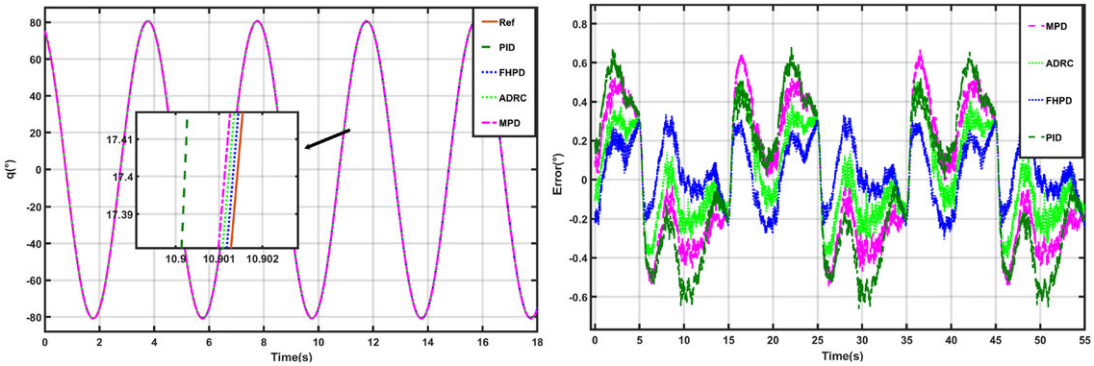
1. Transient performance in the simulation experiments in Figure 7 illustrates the effect of the FHPD control strategy on the disc motor's response to a step signal. The FHPD controller not only achieves rapid stabilization but also maintains high control precision, with errors being smaller and exhibiting superior convergence speed compared to other controllers.
2. Steady-state Performance, Figure 8, compares the performance of the three control strategies in the sinusoidal signal tracking experiment. Additionally, as can be seen from Figure 8, the FHPD control strategy outperforms PID and MPD in terms of accuracy, which is consistent with the simulation analysis. The highest tracking errors typically occur when the disc motor's speed is near zero, mainly due to the imprecision of the position sensor and static friction. The experimental results indicate that there is almost no difference in control current among the three approaches.

https://doi.org/10.1017/S026357472510266X Published online by Cambridge University Press



A comparison of experimental outcomes — Angular error tracking step signals

Figure 7. *The experiment results of step response analysis.*



A comparison of experimental outcomes — Angular error tracking sin signals

Figure 8. *Sinusoidal response analysis.*

Figure 9 presents a comparative analysis of current waveforms for the FHPD, MPD, and PID controllers during experimental operation. The results indicate that the FHPD controller achieves significantly reduced current oscillations compared to the other methods, demonstrating enhanced stability and energy efficiency. Notably, the FHPD exhibits lower peak currents and reduced fluctuations, which directly translate to decreased energy consumption. This improved performance is attributed to the FHPD's optimized control strategy, which minimizes unnecessary power usage while maintaining precise tracking. The figure clearly illustrates the practical benefits of the FHPD controller in real-world applications.

Table III presents a summary and comparison of the experimental findings. This comparison includes key performance indicators such as the root mean square error (RMSE), maximum error (MAXE), minimum error (MINE), and the range of error (Δ_θ).

$$MAXE = \max\left(|\theta_i|\right) \tag{45}$$

$$MINE = \min\left(|\theta_i|\right) \tag{46}$$

$$RMSE = \sqrt{\frac{1}{n}\sum_{i=1}^{n}\theta_i^2} \tag{47}$$

$$\Delta_\theta = \theta_{MAXE} - \theta_{MINE} \tag{48}$$

https://doi.org/10.1017/S026357472510266X Published online by Cambridge University Press

Table III. *Comparison of control response performance of different control methods.*

Performance	**RMSE (deg)**	**MAXE (deg)**	**MINE (deg)**	Δ_θ
PID	0.4146	0.6580	−0.6300	1.2880
MPD	0.3558	0.6550	−0.5380	1.1930
ADRC	0.1545	0.3940	−0.3920	0.7860
FHPD	0.0707	0.3230	−0.2090	0.5320
Improvement (PID)	82.95%	50.92%	66.83%	58.70%
Improvement (MPD)	80.13%	50.69%	52.22%	55.41%
Improvement (ADRC)	54.24%	18.02%	46.68%	32.32%

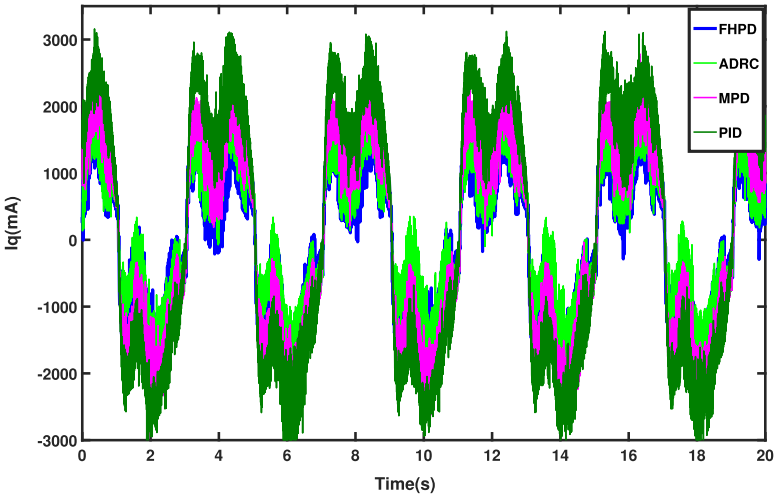
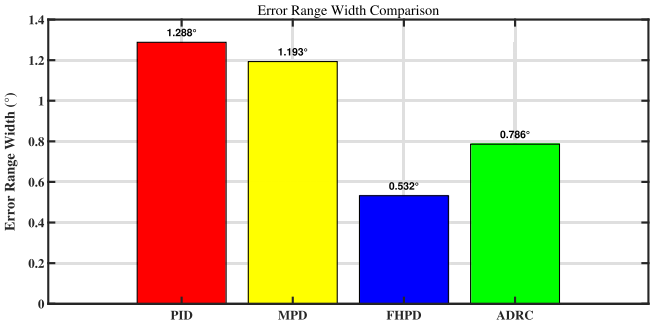


Figure 9. *Current waveform comparison.*

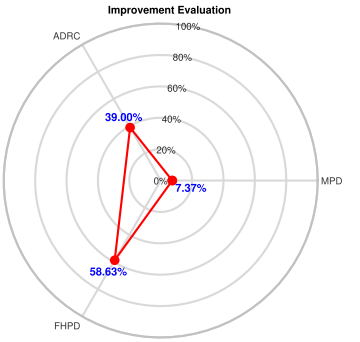
The variable n indicates the total number of samples, while θ_i signifies the tracking error for each individual sample i. The analysis indicates that the FHPD controller exhibits significant improvements in tracking accuracy and robustness compared to the PID, MPD, and ADRC methods. The FHPD controller demonstrates a substantial reduction in both RMSE and MAXE, along with a narrower error range, which underscores its enhanced performance and stability. These improvements are particularly important for maintaining consistent performance across various experimental conditions, highlighting the FHPD controller's effectiveness in handling uncertainties such as tracking errors.

To comprehensively evaluate the performance of the FHPD controller against traditional PID and MPD controllers, we have incorporated several illustrative figures. The left figure in Figure 10 presents a bar chart comparing the tracking error range width from the sinusoidal tracking experiment, clearly highlighting the disparities in error ranges among the three methods. The results demonstrate that the proposed FHPD controller achieves a tracking error of 0.532°, representing a 58.70% reduction compared to the traditional PID controller (1.288°) and a 55.41% reduction compared to the traditional MPD controller (1.193°). Additionally, the FHPD controller outperforms ADRC (0.786°) by reducing the tracking error by 32.32%. These findings highlight the superior performance of the FHPD controller in tracking accuracy. The right figure in Figure 11 offers a radar chart depicting the improvement percentages of the FHPD method relative to the others, visually emphasizing its significant performance enhancement. The left figure in Figure 11 displays a bar chart contrasting the stability difference width between simulation and experimental results in the step response test, demonstrating the FHPD controller's consistent performance across both scenarios. The right figure in Figure 10 provides a bar chart of the difference percentages between simulation and experimental results for the three methods, further

https://doi.org/10.1017/S026357472510266X Published online by Cambridge University Press

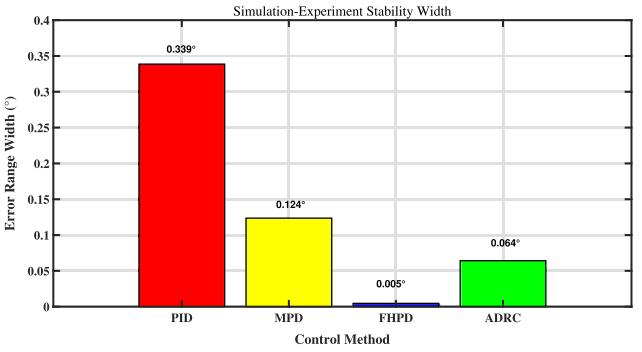


Tracking Error Range Comparison

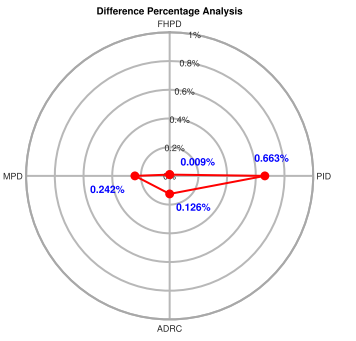


Improvement percentage Comparison

Figure 10. *Tracking error and improvement analysis.*



Simulation-Experiment Stability Width



Simulation-Experiment Difference percentage

Figure 11. *Simulation-experiment comparison.*

substantiating the reliability of the FHPD controller. Together, these visual aids effectively elucidate the performance variations among different control methods and underscore the superiority of the proposed FHPD controller.

4. Conclusion

This study proposes a fractional-order hybrid PD (FHPD) control framework that synergistically integrates mechanical dynamics modeling with adaptive robustness mechanisms. Lyapunov stability analysis formally guarantees the boundedness of system uncertainties and disturbances. Through comprehensive simulations and experimental validations under trajectory tracking tasks, the FHPD demonstrates 58.70% reductions in tracking error range compared to PID, respectively, significantly outperforming conventional methods in precision control. Notably, the experimental results maintain exceptional consistency with simulations, exhibiting less than 0.009% deviation in step response steady-states. These quantifiable improvements confirm the controller's dual advantages in dynamic accuracy and implementation reliability. The proposed methodology provides a generalized solution for nonlinear systems with inherent uncertainties, particularly effective in load fluctuation mitigation. Future work will extend this architecture to multi-DOF robotic systems to explore its scalability in complex operational scenarios.

Author contributions. Xiaoli Liu, Youli Hu and Faliang Wang conceived and designed the study. Shengchao Zhen conducted data gathering. Ye-Hwa Chen performed statistical analyses. Xiaoli Liu, Youli Hu and Faliang Wang wrote the article.

https://doi.org/10.1017/S026357472510266X Published online by Cambridge University Press

Funding statement. This work was supported in part by the National Natural Science Foundation of China (Grant No. 52305084 and 52175083); in part by the Natural Science Foundation of Anhui Province (Grant No.2308085QE161); in part by the Fundamental Research Funds for the Central Universities (JZ2024HGTG0300); in part by the University Synergy Innovation Program of Anhui Province (GXXT-2023-108); in part by the University-Local Government Collaborative Industry Innovation Guidance Fund Project (JZ2024YDZJ0038).

Competing interest. The authors declare no potential conflicts of interest with respect to the research, authorship, and/or publication of this article.

Ethical approval. None.

References

[1] T. Xue, Z. Wang, T. Zhang, M. Zhang and Z. Li, "The Control System for Flexible Hip Assistive Exoskeleton," **In:** *2018 IEEE International Conference on Robotics and Biomimetics (ROBIO)* (2018) pp. 697–702.
[2] T. Xue, Z. Wang, T. Zhang, M. Zhang and Z. Li, "Adaptive oscillator-based robust control for flexible hip assistive exoskeleton," *IEEE Rob. Autom. Lett.* **4**(4), 3318–3323 (2019).
[3] Q. Wu, X. Wang, F. Du and X. Zhang, "Design and control of a powered hip exoskeleton for walking assistance," *Int. J. Adv. Rob. Syst.* **12**(3), 18 (2015).
[4] W. Wei, S. Zha, Y. Xia, J. Gu and X. Lin, "A hip active assisted exoskeleton that assists the semi-squat lifting," *Appl. Sci.* **10**(7), 2424 (2000).
[5] T. Zhang, M. Tran and H. Huang, "Design and experimental verification of hip exoskeleton with balance capacities for walking assistance," *IEEE/ASME Trans. Mechatron.* **23**(1), 274–285 (2018).
[6] Q. Zhang, V. Nalam, X. Tu, M. Li, J. Si, M. D. Lewek and H. H. Huang, "Imposing healthy hip motion pattern and range by exoskeleton control for individualized assistance," *IEEE Rob. Autom. Lett.* **7**(4), 11126–11133 (2022).
[7] S. Zhen, Z. Zhao, X. Liu, F. Chen, H. Zhao and Y. H. Chen, "A novel practical robust control inheriting pid for scara robot," *IEEE Access.* **8**, 227409–227419 (2020).
[8] T.-J. Ha, J. Lee and J. H. Park, "Robust Control by Inverse Optimal PID Approach for Flexible Joint Robot Manipulator," **In:** *2007 IEEE International 410 Conference on Robotics and Biomimetics (ROBIO)* (2007) pp. 336–341.
[9] T. A. Khaled, O. Akhrif and I. A. Bonev, "Dynamic path correction of an industrial robot using a distance sensor and an ADRC controller," *IEEE/ASME Trans. Mechatron.* **26**(3), 1646–1656 (2020).
[10] S. Zhong, Y. Huang and L. Guo, "An ADRC-based pid tuning rule," *Int. J. Robust Nonlinear Control.* **32**(18), 9542–9555 (2022).
[11] X. Li, W. Ai, Z. Gao and S. Tian, "Robust Adrc for Nonlinear Time-Varying System with Uncertainties," **In:** *2017 6th Data Driven Control and Learning Systems (DDCLS)* (IEEE) (2017) pp. 350–356.
[12] K. Rsetam, Z. Cao and Z. Man, "Design of robust terminal sliding mode control for underactuated flexible joint robot," *IEEE Trans. Syst. Man Cybern. Syst.* **52**(7), 4272–4285 (2022).
[13] A. Aswani, H. Gonzalez, S. S. Sastry and C. Tomlin, "Provably safe and robust learning-based model predictive control," *Automatica.* **49**(5), 1216–1226 (2013).
[14] T. Zeng, A. Mohammad, A. G. Madrigal, D. Axinte and M. Keedwell, "A robust human–robot collaborative control approach based on model predictive control," *IEEE Trans. Ind. Electron.* **71**(7), 7360–7369 (2023).
[15] D. Wang, W. Wei, Y. Yeboah, Y. Li and Y. Gao, "A robust model predictive control strategy for trajectory tracking of omni-directional mobile robots," *J. Intell. Rob. Syst.* **98**(2), 439–453 (2020).
[16] R. Zhao, L. Wu and Y.-H. Chen, "Robust control for nonlinear delta parallel robot with uncertainty: An online estimation approach," *IEEE Access.* **8**, 97604–97617 (2020).
[17] S. Hwang, S. H. Park, M. Jin and S. H. Kang, "A robust control of robot manipulators for physical interaction: Stability analysis for the interaction with unknown environments," *Intell. Serv. Rob.* **14**(3), 471–484 (2021).
[18] F. Qin, H. Zhao, S. Zhen, H. Sun and Y. Zhang, "Lyapunov based robust control for tracking control of lower limb rehabilitation robot with uncertainty," *Autom. Syst.* **18**, 76–84 (2020).
[19] C. Dawson, Z. Qin, S. Gao and C. Fan, "Safe Nonlinear Control Using Robust Neural Lyapunov-Barrier Functions," **In:** *2022 Conference on Robot Learning. PMLR.* (2022) pp. 1724–1735.
[20] B. Yao and C. Jiang, "Advanced Motion Control: From Classical PID to Nonlinear Adaptive Robust Control," **In:** *2010 11th IEEE International Workshop On Advanced Motion Control (AMC)* (IEEE) (2010) pp. 815–829.
[21] J. Moreno-Valenzuela, Y. Quevedo-Pillado, R. Pérez-Aboytes and L. González-Hernández, "Lyapunov-based adaptive control for the permanent magnet synchronous motor driving a robotic load," *J. Circuits Syst. Comput.* **26**(11), 1750168 (2017).
[22] F. Marques, P. Flores, J. P. Claro and H. M. Lankarani, "A survey and comparison of several friction force models for dynamic analysis of multibody mechanical systems," *Nonlinear Dyn.* **86**, 1407–1443 (2016).
[23] E. Pennestr'ı, V. Rossi, P. Salvini and P. P. Valentini, "Design and experimental verification of hip exoskeleton with balance capacities for walking assistance," *Nonlinear Dyn.* **83**, 1785–1801 (2016).
[24] X. Shao, N. Liu, Z. Wang, W. Zhang and W. Yang, "Neuroadaptive integral robust control of visual quadrotor for tracking a moving object," *Mech. Syst. Signal Process.* **136**, 106513 (2020).

https://doi.org/10.1017/S026357472510266X Published online by Cambridge University Press

[25] Y. W. Tang, H. X. Sun, X. Li and J. Z. Song, "Nonlinear Friction Modeling for Modular Robot Joints," **In:** *MECHANICS AND MECHANICAL ENGINEERING: Proceedings of the 2015 International Conference (MME2015)* (2016) pp. 908–915.
[26] J.-J. E. Slotine and W. Li, "Applied nonlinear control," *Appl. Nonlinear Control.* **199**(705) (1991).
[27] M. Corless and G. Leitmann, "Continuous state feedback guaranteeing uniform ultimate boundedness for uncertain dynamic systems," *IEEE Trans. Autom. Control.* **26**(5), 1139–1144 (1981).
[28] C. P. Bechlioulis and G. A. Rovithakis, "Adaptive control with guaranteed transient and steady state tracking error bounds for strict feedback systems," *Automatica.* **43**(2), 31 (2009).

Cite this article: X. Liu, Y. Hu, F. Wang, S. Zhen and Y. Chen (2025). "Robust control based on Lyapunov stability theory for the joint modules in hip-assist exoskeleton robots", Robotica **43**, 3959–3975. https://doi.org/10.1017/S026357472510266X

https://doi.org/10.1017/S026357472510266X Published online by Cambridge University Press